ARTICLE IN PRESS

npj 2D Materials and Applications

https://doi.org/10.1038/s41699-026-00676-3

Article in Press

Phase-controlled synthesis and two-dimensional electronic transport of ultrathin tungsten carbide platelets

Received: 22 July 2025

Accepted: 3 February 2026

Cite this article as: Sredenschek, A.J., Sanchez, D., Wang, J. *et al.* Phase-controlled synthesis and two-dimensional electronic transport of ultrathin tungsten carbide platelets. *npj 2D Mater Appl* (2026). https://doi.org/10.1038/s41699-026-00676-3

Alexander J. Sredenschek, David Sanchez, Jiayang Wang, Da Zhou, Le Yi, Zhuohang Yu, Morteza Kayyalha, Susan B. Sinnott & Mauricio Terrones

We are providing an unedited version of this manuscript to give early access to its findings. Before final publication, the manuscript will undergo further editing. Please note there may be errors present which affect the content, and all legal disclaimers apply.

If this paper is publishing under a Transparent Peer Review model then Peer Review reports will publish with the final article.

ARTICLE IN PRESS

© The Author(s) 2026. **Open Access** This article is licensed under a Creative Commons Attribution-NonCommercial-NoDerivatives 4.0 International License, which permits any non-commercial use, sharing, distribution and reproduction in any medium or format, as long as you give appropriate credit to the original author(s) and the source, provide a link to the Creative Commons licence, and indicate if you modified the licensed material. You do not have permission under this licence to share adapted material derived from this article or parts of it. The images or other third party material in this article are included in the article's Creative Commons licence, unless indicated otherwise in a credit line to the material. If material is not included in the article's Creative Commons licence and your intended use is not permitted by statutory regulation or exceeds the permitted use, you will need to obtain permission directly from the copyright holder. To view a copy of this licence, visit http://creativecommons.org/licenses/by-nc-nd/4.0/.

ARTICLE IN PRESS

Title: Phase-controlled synthesis and two-dimensional electronic transport of ultrathin tungsten carbide platelets

Authors: Alexander J. Sredenschek[1,2], David Sanchez[2,3], Jiayang Wang[2,3], Da Zhou[1,2], Le Yi[1], Zhuohang Yu[2,3], Morteza Kayyalha[4], Susan B. Sinnott[2,3,5,6], Mauricio Terrones[1,2,3,5,*]

Affiliations

1. Department of Physics, The Pennsylvania State University, University Park, PA, USA.

2. Center for 2D and Layered Materials, The Pennsylvania State University, University Park, PA, USA.

3. Department of Materials Science and Engineering, The Pennsylvania State University, University Park, PA, USA.

4. Department of Electrical Engineering, The Pennsylvania State University, University Park, PA, USA.

5. Department of Chemistry, The Pennsylvania State University, University Park, PA, USA.

6. Institute for Computational and Data Science, The Pennsylvania State University, University Park, PA

*Corresponding author: Mauricio Terrones (mut11@psu.edu)

ARTICLE IN PRESS

Abstract

The transition metal carbide (TMC) family has been previously studied for various catalytic, mechanical, and electronic applications, and recently TMCs have been isolated into the ultrathin limit. A bottom-up approach has been developed to synthesize non-layered, ultrathin TMCs (UThTMCs). In this work, liquid metal assisted chemical vapor deposition is used to control the growth of different phases of tungsten carbide. In particular, WC and W_2C single crystal nanoplates are synthesized when using copper and gallium, respectively, as the tungsten diffusion barrier. First principles calculations confirm the stability found experimentally in the two synthesized carbide phases. We also report the first low temperature measurements of electronic transport in WC below 300 mK and ultrathin W_2C down to 1.8 K. We find that WC does not enter a superconducting state, while UThTMCs of W_2C enter a 2D superconducting state below 2.8 K. Our results provide new ground on the synthesis of other UThTMCs with controlled crystal phase. Given the richness of phases among metal carbides and the related transition metal nitride family, further research will be motivated by this work to isolate novel carbide and nitride phases in this ultrathin limit. Finally, it is important to note that the electronic transport of UThTMCs follows a 2D regime and further systems should be evaluated and compared, especially the superconducting phases. These UThTMCs and their heterointerfaces could find important applications in electrocatalysis, carbide plasmonics, transparent conducting films, and materials for effective radiation shielding due to their high density and ability to absorb neutrons and gamma rays.

Introduction

Transition metal carbides (TMCs) and nitrides have historically received attention for applications that utilize the high hardness, chemical stability, and catalytic activity of these compounds in bulk crystal, powder, and thin film morphologies.[1–3] This family entered into the ultrathin spotlight under two synthesis paradigms, with the isolation of two dimensional (2D) carbides and nitrides in layered, van der Waals (vdW) phases, termed MXenes,[4–6] and non-layered phases, termed ultrathin TMCs (UThTMCs).[7] MXenes

are commonly isolated through chemical exfoliation *via* selective etching in hydrofluoric acid[8,9] or molten salts,[10] though a recent bottom-up approach using chemical vapor deposition (CVD) has been developed for MXene synthesis.[11] The majority of MXene studies use the key MAX phase ingredient for top-down MXene synthesis. In the case of tungsten-based MXenes, ternary tungsten-based ternary MAX phases are not stable and only one binary tungsten carbide MXene has been isolated to date from quaternary tungsten-based MAX phases.[12] The scarcity of suitable tungsten-based MAX phases limits the exploration of ultrathin tungsten carbide properties which have been shown to be competitive candidates for applications in electrocatalysis[13] and a platform for exploring dimensionality effects in the ultrathin limit like what has been in done in similar TMC systems.[7,14] Additionally, probing electronic transport is frustrated by small grain size, non-uniform layer terminations, and interlayer intercalants in MXene powders.[15] One way to address these issues is to seek alternative synthesis routes for highly crystalline UThTMCs to investigate phase dependent electrocatalysis[16] and low dimensional electronic transport properties.

Liquid metal-assisted chemical vapor deposition (LMCVD) is an approach that has previously been used to grow high purity, single crystal, non-layered UThTMC nanoplatelets such as Mo_2C,[7,14,17–19] WC,[20,21] NbC,[22] TaC,[23] and VC[24] which are all distinct from MXenes. The high degree of crystallinity and purity of these platelets facilitates accurate and detailed property characterization, such as catalysis and electronic transport properties. Such systems also have been used for the generation of high-quality heterostructures and have potential to function as templates for integration with layered systems such as the transition metal dichalcogenide family.[25,26] LMCVD-synthesized Mo_2C exhibits thickness- and phase-dependent superconducting transitions operating in the clean limit, and anisotropic critical field behavior characteristic of 2D superconductivity;[7,14] ultrathin semimetallic WC shows anisotropic magnetoresistance[20] consistent with predicted and measured non-trivial topological features;[27] and as-grown ultrathin NbC platelets exhibit a Josephson network array.[22] While at least one carbide phase from all Group-V and Group-VI TMCs has been grown using LMCVD, to the best of our knowledge there have not been detailed studies on phase control of TMCs beyond Mo_2C with LMCVD. Phase control is critical towards controlling the properties of these UThTMCs. For example, in the tungsten carbide system, hexagonal WC is a semimetal,[28] while W_2C is a conventional type-II superconductor as shown in early studies of the bulk carbides.[29,30] 2D superconducting features have been well-studied in ultrathin Mo_2C platelets synthesized through LMCVD but not yet in ultrathin W_2C owing to challenges of phase control.

The LMCVD approach shares features with conventional CVD, but the key difference is the role of the substrate. In LMCVD, the substrate consists of a bilayer stack of two metals—the bottom consists of the target transition metal in the TMC, and the top layer is an immiscible, low-carbon-solubility metal. This substrate is then heated above the melting point of the diffusion barrier under a mixture of gaseous hydrocarbons (*e.g.* CH_4) and reducing agents (*e.g.* H_2). The liquefied top layer functions as a diffusion barrier for both carbon species and transition metal atoms from the bottom layer of the substrate. Reaction temperature, time, gas concentrations, and diffusion barrier thickness are all parameters that can tune the diffusion of carbon species and transition metal atoms through the barrier and consequently, the nucleation and growth of the ultrathin TMC platelets. Previous works have typically used copper as the diffusion barrier,[7,14,18,20,22,31] though copper/zinc alloys,[32] gallium,[21] gold,[33] and indium[19] have also been used. In previous LMCVD studies of UThTMCs, typically one crystalline structure is formed, but tuning the CH_4 to H_2 ratio can promote the formation of both orthorhombic (Pbcn) and hexagonal ($P6_3/mmc$) Mo_2C grown on copper/molybdenum bilayer substrates.[14,34] Because TMC properties are closely coupled to the

ARTICLE IN PRESS

crystal structure,[35,36] control over the crystal structure and morphology (*e.g.* platelet thickness and lateral dimension) of UThTMCs is critical for their utilization in applications such as electrocatalysis, plasmonics, radiation protection, and for electronic transport studies. While ultrathin Mo_2C has received much attention, few studies have focused on tungsten carbide with respect to phase or polymorph modification.

In the tungsten carbide system,[20,21] there has been little study on the effects of growth temperature, time and gas ratios on the lateral size and thickness of the platelets, aspects that are important towards understanding aspects of the tungsten carbide growth mechanism. Additionally, there has been no focus on phase control in LMCVD-synthesized tungsten carbides. In this study we probe the LMCVD synthesis parameter space of tungsten carbide by modification of the diffusion barrier. We find that using copper and gallium produces two distinct tungsten carbide phases in nanoplatelet morphologies following the work of two recent reports,[20,21] and we offer explanations for the formation of two distinct phases. We carry out structural, chemical, and electronic property characterization of both WC ($P\bar{6}m2$) and W_2C (Pbcn) nanoplatelets. Here we report the first, to the best of our knowledge, electronic transport properties of ultrathin WC below 300 mK and ultrathin W_2C to 1.8 K to assess the superconducting features here. We also carry out first-principles density functional theory (DFT) calculations coupled with thermochemical data to understand the thermodynamic conditions under which these two phases may be stabilized. These results provide a foundation for extending the LMCVD approach to isolate new UThTMCs, control TMC phase formation in the ultrathin limit, and tailor UThTMC morphology for application in catalysis, radiation protection, and electronic transport.

Results

A schematic of the LMCVD process is shown in Figure 1a. Two substrates are used to synthesize tungsten carbide: copper foil on tungsten foil (termed Cu/W) and a gallium shot (liquid) on tungsten foil (termed Ga/W). Each substrate rests at the center of an atmospheric pressure quartz tube furnace where varying flows of Ar, H_2, and CH_4 are controlled at set temperatures. In the LMCVD process, the substrate temperature must exceed that of the diffusion barrier melting point (1085°C for copper and 30°C for gallium) and ensure sufficient methane pyrolysis in the argon/hydrogen atmosphere. Typically, CH_4 pyrolysis onset in an inert environment occurs at temperatures greater than 1200°C, though the introduction of catalysts and hydrogen can lower this temperature.[37,38] For Cu/W substrates, we choose a growth temperature of 1090°C, and for Ga/W substrates we use 1000°C. We first identify that the platelets grown on Cu/W yield primarily triangular platelets, while those on Ga/W substrates yield hexagonal ultrathin platelets as seen in Figure S1a,b. We perform atomic force microscopy (AFM) measurements on the platelets after transferring them to SiO_2/Si substrates using a polymethyl methacrylate (PMMA)-assisted wet transfer. The platelets shown for WC and W_2C have respective thicknesses of around 40 nm and 20 nm (Figure S1c-f). We note that both the WC and W_2C platelets host surface impurities on the micron scale. In the case of both systems, the carbon residues from the PMMA transfer may explain some of these features. The ribbon-like features in WC likely correspond to graphene, and the thick aggregates on the W_2C platelet are likely gallium oxide, both of which features will be discussed at a later point in the article.

We also show representative flake statistics in Figure S2. From optical microscopy images, we measure the size of the W_2C hexagonal flakes (Ga/W substrates), and WC triangular platelets (Cu/W substrates) shown in Figures S2a and S2b, respectively. For W_2C hexagonal flakes, we find an average lateral size of about 2.3 μm and standard deviation of 0.9 μm; for WC triangular flakes we find an average lateral size

(triangle side length) of about 3.8 µm and standard deviation of 1.6 µm. The thickness distribution of W_2C and WC flakes, measured from atomic force microscopy of samples transferred onto SiO_2/Si, are shown in Figure S2c. We find a mean nanoplatelet thickness of 50 nm and 43 nm for W_2C and WC, respectively. The standard deviations for the platelet thicknesses are quite large with about 26 nm and 23 nm for W_2C and WC, respectively, indicating room for improvement for thickness control over these nanoplates.

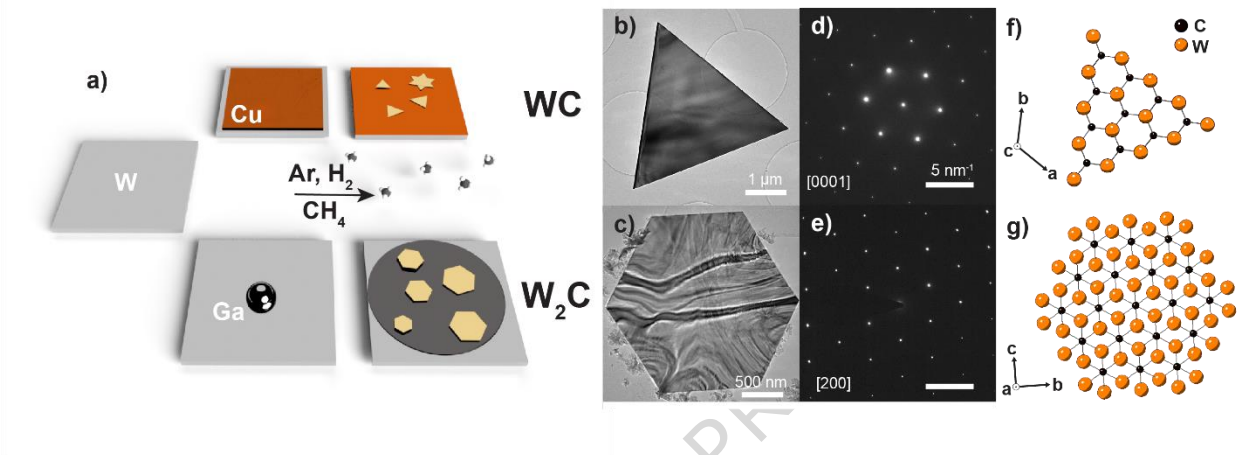

Figure 1: Synthesis and planar crystal structure analysis of WC and W_2C. a) Schematic of substrate configurations used for the LMCVD process, highlighting the formation of WC nanoplates with Cu/W substrates and W_2C nanoplates with Ga/W substrates. b-c) Planar TEM images of WC and W_2C platelets, respectively, with their respective d-e) SAED patterns (5 nm^{-1} scalebar). The WC pattern is consistent with the [0001] zone axis of the WC ($P\bar{6}m2$) phase, and the W_2C pattern is consistent with the [200] zone axis of the W_2C (Pbcn) phase. f-g) Crystal structures of WC and W_2C viewed from the zone axes of the SAED patterns.

We next assess the crystal structure and degree of crystallinity of the tungsten carbide platelets. Shown in Figure 1b-c are planar transmission electron microscopy (TEM) images of tungsten carbide platelets from Cu/W and Ga/W substrates, respectively. These TEM images show a triangular platelet grown on Cu/W and a hexagonal platelet grown on Ga/W. The selected area electron diffraction (SAED) patterns shown in Figure 1d-e indicate that the triangular and hexagonal platelets are single crystalline. We measured the interplanar spacings of the first order diffraction peaks from the SAED patterns, and we find these values are 2.522 Å for tungsten carbide grown on Cu/W and 2.605 Å for tungsten carbide grown on Ga/W. Comparing these measurements to JCPDS standard references, we find that the interplanar spacings for crystals grown on Cu/W match closely to the (100) planes of WC ($P\bar{6}m2$) with d_{100} = 2.517 Å (PDF card no. 00-051-0939), and the spacings for crystals on Ga/W match closely to the (021) and (002) planes of W_2C (Pbcn) with d_{021} = 2.606 Å and d_{002} = 2.590 Å (PDF card no. 04-003-6377). We then carry out high-resolution TEM (HRTEM) on WC (Figure S3a) and W_2C (Figure S3d). We match the W_2C polymorph to the orthorhombic configuration (Pbcn) owing to the appearance of forbidden reflections in the Fourier transform of the HRTEM images (Figure S3b,e) matching with simulated SAED patterns (Figure S3c,f).

We identify the zone axes of the SAED patterns as [001] for WC and [200] for W_2C, respectively. Moreover, we show in Figure 1f and 1g the atomic models of WC ($P\bar{6}m2$) and W_2C (Pbcn) along these zone axes and the plane terminations of the platelet facets, oriented along with the TEM and SAED images. The planar SAED analysis suggests that the triangular tungsten carbide nanoplates on Cu/W are the monocarbide WC ($P\bar{6}m2$) and the hexagonal nanoplates grown on Ga/W are the semicarbide W_2C in the orthorhombic polymorph (Pbcn). We note however that these planar SAED patterns can be difficult to differentiate, and this difficulty reflects the historical challenges in crystal structure identification of TMCs.[39] It was recently

ARTICLE IN PRESS

reported[21] that tungsten carbide grown on Ga/W was the monocarbide ($P\bar{6}m2$) on the basis of planar SAED patterns. To corroborate these findings from planar SAED and to resolve discrepancies in the literature, we carry out X-ray diffraction (XRD) and cross-sectional TEM.

The XRD patterns of both as-grown WC/Cu/W and W_2C/Ga/W, as well as these samples transferred onto SiO_2/Si are shown in Figure 2a. First, the substrate contributes in the as-grown samples with the body-centered-cubic tungsten metal (200) peak; the SiO_2/Si substrate contributes in this range at ~33°, corresponding to a forbidden reflection of the (400) planes of SiO_2/Si. In the WC/Cu/W pattern, we can identify three contributions to the observed diffraction peaks: WC, W_2C, and tungsten (body-centered cubic). The tungsten originates from the tungsten foil substrate, and the W_2C originates from tungsten-rich features (aggregates) that are distinct from the triangular platelets as seen in the dark particle-like features in the optical microscopy image in Figure S1a. We note however that upon transfer in the WC/SiO_2/Si spectrum, these W_2C peaks are still present, namely from the (200) and (121) planes. To determine the origin of this signal, we carried out Raman spectroscopy on both WC and W_2C platelets. Raman spectra under 532 nm excitation of as-grown hexagonal W_2C/Ga/W (Figure S4a) and triangular WC/Cu/W (Figure S4b) platelets are shown in Figure S4c. We find that the W_2C shows three prominent Raman modes at 106, 117, and 140 cm^{-1}, while the WC shows no Raman modes in this region. Using these spectra as a reference, we examine the Raman response of features in the as-grown WC/Cu/W and transferred WC/SiO_2/Si samples. Figure S5a shows an optical microscope image of the carburized Cu/W with regions labelled according to where Raman spectra were taken shown in Figure S5a. This region was selected to highlight the small aggregate features, rather than the triangular WC nanoplates. The copper substrate in spectrum g1 shows no peaks, while those in g2, g3, and g5 have Raman modes that match those observed in Figure S4c. We also note that in Region g4 with the discolored patch, there is copper oxide Raman signal.[40] These Raman measurements show that W_2C originates from these small, sub-micron-sized particulates on the as-grown WC/Cu/W. To determine the origin of the W_2C peaks in the XRD scan of WC transferred onto SiO_2, we then measure Raman spectra of select regions of WC/SiO_2/Si in Figure S5c-d. Spectra from regions t1 through t4 show Raman signals similar to the as-grown sample, particularly regions g2, g3, and g5 in Figure S5b. These small aggregates show Raman peaks at the same positions as those observed for the hexagonal W_2C platelets on gallium (Figure S4c).

We then estimate the proportion of W_2C that is formed during the synthesis of tungsten carbide on Cu/W substrates. To do this, we measured OM images similar to the one shown in Figure S1a. Using ImageJ[41], we count the number of triangular nanoplates (WC) and small aggregates (W_2C) using thresholding and measure their respective areas. Across eight representative OM images collected, from Cu/W substrates, containing both triangular WC platelets and aggregates of W_2C, we find average area coverages of about 2.4% for triangular WC platelets and 0.088% for W_2C aggregates, with respective standard deviations of 1.0% and 0.0087%. The nucleation density is estimated by counting the number of triangular WC platelets and W_2C aggregates and dividing by the area of the optical image. In units of number of triangular tungsten carbide nanoplates (for WC) or number of tungsten carbide aggregates (for W_2C) per $(100\ \mu m)^2$ = 10,000 μm^2 we find average nucleation densities of 21 for triangular WC platelets and about 34 for W_2C aggregates (respective standard deviations of 10 and 7). While the nucleation density of both phases is similar, the area coverages are different by an order of magnitude. We estimate the contributions of each tungsten carbide phase to the total tungsten carbide content by examining the area coverages. The contribution of triangular WC to the tungsten carbide coverage is approximated by taking the ratio of (average) WC coverage to the combined WC and W_2C coverage, as (100%)*2.4/(2.4+0.088) ≈ 96%. While

this estimate does not take into account the relative volume fractions of the two phases, the majority of the lateral coverage arises from triangular WC nanoplates on copper substrates. With the origin of the W_2C signal in the XRD spectra of WC understood and with estimates on the relative quantity of phases on Cu/W substrates, we next turn to the analysis of the WC peaks.

We identify three reflections corresponding to WC in the as-grown and transferred samples: (001), (100), and (101). The existence of multiple planes of the WC could result from nanoplatelets that are not flat with respect to the XRD stage. This is a consequence of the copper substrate having local variations in height after the solidification of liquid copper after the growth step (Figure S1a). After investigation of the SAED pattern for the WC/Cu/W system, we confirm that the zone axis is [001], observed in the XRD pattern. From the (001) position we measure d_{001} = 2.83 Å (PDF card no. 00-051-0939: d_{001} = 2.84 Å). We next turn to the W_2C/Ga/W and W_2C/SiO_2/Si spectra. Notably, there is no evidence of other tungsten carbide phases in the W_2C samples synthesized from Ga/W substrates. We observe one prominent diffraction peak near 2θ = 38° that corresponds to the [200] zone axis of the SAED pattern for the W_2C polymorphs. We measure an interplanar spacing of d_{200} = 2.36 Å (PDF card no. 04-003-6377: d_{200} = 2.36 Å). The additional (021) peak of W_2C in the as-grown W_2C/Ga/W sample likely originates from platelets embedded in the Ga/W substrate. The crystal structures of WC and W_2C from side profiles ([110] and [010], respectively) are shown in Figure 2b and 2c, respectively. To further confirm these interplanar spacings, we image WC and W_2C with cross-sectional HRTEM (Figure 2d, e). Interplanar spacings between rows of tungsten atoms are measured *via* Fourier transforms (Figure S6b,d) The bright lines are tungsten atoms, and measuring the distance between these layers in the Cu/W and Ga/W systems yields distinct interplanar spacings of 2.83 Å and 2.36 Å, respectively, which match closely to the reference values shown next to the crystal structure drawings of WC and W_2C.

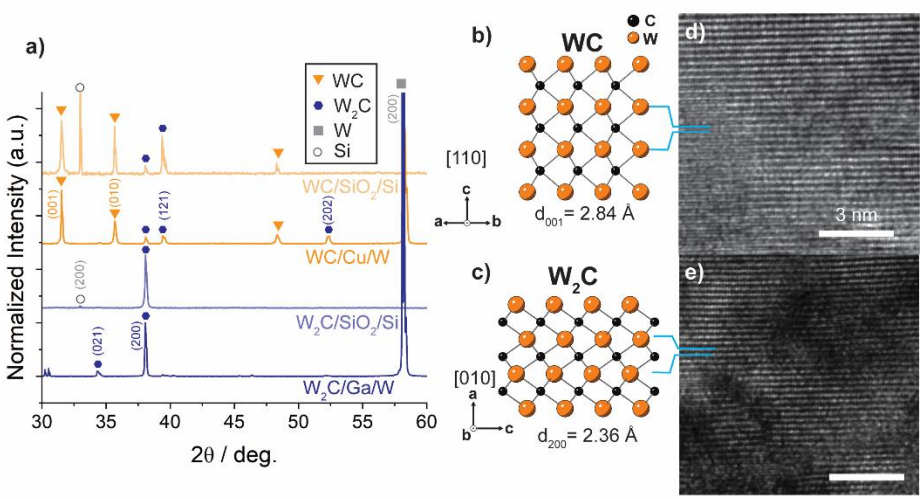

Figure 2: Cross-sectional crystal structure analysis of WC and W_2C. a) XRD spectra of as-grown WC/Cu and W_2C/Ga, and these samples transferred to SiO_2/Si denoted respectively as WC/SiO_2 and W_2C/SiO_2. Miller indices are labelled according to the WC ($P\bar{6}m2$), W_2C (Pbcn), W ($Im\bar{3}m$), and Si ($Fd\bar{3}m$) crystal structures. b-c) Crystal structures of WC and W_2C viewed from [110] and [010], respectively. The interplanar spacings between tungsten atoms are labelled with lines that correspond to d-e) cross sectional HRTEM images of WC and W_2C platelets (scale bars are identical for both HRTEM images).

ARTICLE IN PRESS

With the confirmation of two distinct tungsten carbide phases (WC and W_2C) in the nanoplate morphology, we return to the planar TEM and SAED data for the W_2C. A closer look at the SAED pattern reveals weak intensity diffraction peaks. These kinematically-forbidden reflections may arise in the Pbcn polymorph of W_2C due to the presence of defects such as stacking faults and vacancies or dynamic scattering events from screw axes.[41] With this in mind, we conclude that the W_2C crystallizes in the Pbcn polymorph. This analysis confirms that modification of the diffusion barrier in the LMCVD process yields two distinct tungsten carbide phases in the nanoplatelet morphologies.

To investigate the chemical composition of the crystals, we perform energy dispersive X-ray spectroscopy (EDS) on the WC and W_2C nanoplates from Cu/W and Ga/W, respectively. Scanning transmission electron microscope (STEM) images of WC and W_2C are shown in Figure 3a and 3d. In WC nanoplates, we find that both tungsten (Figure 3b) and carbon (Figure 3c) signals are uniform across the platelet. For W_2C, we observe curvature, reflected in slightly non-uniform tungsten (Figure 3e) and carbon (Figure 3f) distributions in the EDS map. As for the W_2C crystals, the other primary elements observed are gallium and oxygen with maps shown in Figure 3g and 3h, respectively. For both WC and W_2C, we do not observe any other elemental contributions in the entire regions, evidenced by the total EDS spectra shown in Figure 3i. The gallium and oxygen signals in W_2C originate from gallium oxide that was produced during the synthesis process and was transferred along with the tungsten carbide crystals to the TEM grid. We notice that such crystallites have overlapping gallium and oxygen signals. The exact composition of the oxide cannot be verified across the entire platelet, though in some regions the Ga:O ratio is near 2:3, expected for the thermodynamically stable gallium oxide Ga_2O_3. The origin of gallium oxide may result from oxygen contamination from the gas cylinders, the quartz tube, and/or the alumina crucible. Such low levels of oxygen contamination could still influence the gallium substrate, considering that gallium oxide can form at sub-ppm levels of O_2.[42] On the other hand, WC does not appear to host a detectable oxygen content. While the sources of potential oxygen contamination are the same in the synthesis approaches for WC/Cu/W and W_2C/Ga/W, there are two key differences arising from the substrates. The

ARTICLE IN PRESS

first is that the formation of gallium oxide is more favorable than copper,[43,44] and the second is that copper can more-readily form graphitic carbon which may act as a barrier for oxidation of the copper surface.

Figure 3: Chemical composition analysis of (a-c) WC and (d-f) W_2C platelets from Cu/W and Ga/W substrates, respectively. STEM images of a) WC and d) W_2C platelets illustrate microstructural differences between these two systems, consistent with TEM data shown in Figure 1. The difference in signal across the W_2C platelet could arise from curvature in the platelet from a small thickness or a remaining artifact from growth over the liquid gallium substrate. EDS maps of b) tungsten and c) carbon for the WC platelet

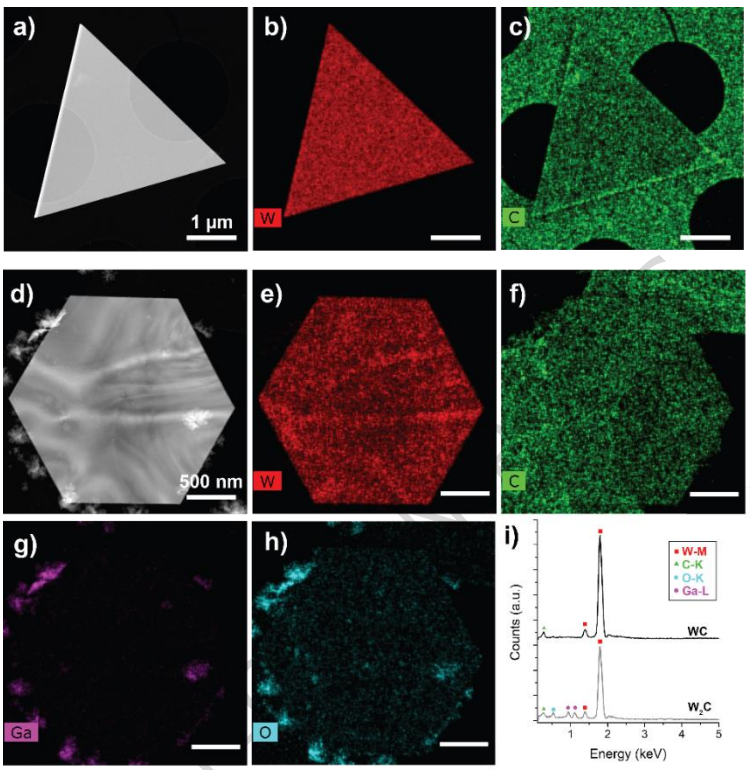

reveal a uniform distribution of these elements. Similar maps are shown for W_2C for e) tungsten and f) carbon. While the carbon signal across the W_2C platelet region suspended over vacuum is uniform, carbon contaminates the remainder of the TEM grid and platelet. Additionally, the tungsten signal is not uniform but instead follows the curvature of the platelet in d). EDS maps of g) gallium and h) oxygen in W_2C reveal the composition of aggregates at the edge of the W_2C platelet. i) EDS spectra of WC and W_2C from the entire regions shown in the STEM images in a) and d), indicating that no other elements than those shown in the EDS maps are present.

To assess the chemical environment of the tungsten and carbon species, we then carried out X-ray photoelectron spectroscopy (XPS). The XPS spectra of the W 4f region are shown in Figure S7. All measured spectra are fit to two pairs of 4f doublets, with one pair at lower binding energies corresponding to metallic tungsten, and the second pair at higher binding energies corresponding to tungsten bonded to carbon. In elemental tungsten, the binding energy of the W $4f_{7/2}$ orbital lies in the range of 31.2-31.8 eV and typically lower in energy than with tungsten bonded to carbon.[45] Binding energies for the $W4f_{7/2}$ position for tungsten bonded to carbon in thin films and bulk powders have been reported at 31.66,[46] 31.8,[47] and 32.2 eV.[48] In W_2C/Ga, the $W4f_{7/2}$ peak positions for elemental W and tungsten bonded to carbon are 31.8 eV and 32.2 eV, respectively; those in WC/Cu are 31.7 eV (elemental W) and 32.3 eV (W-C). We expect to see contributions of metallic tungsten in the as-grown samples in Figure S7a and S7b because the substrates become alloyed with tungsten and the corresponding diffusion barrier. In the samples transferred from the growth substrate onto SiO_2/Si, we still observe signal of both metallic and

ARTICLE IN PRESS

carbon-bonded tungsten in Figure S7c and S7d. For W_2C transferred to SiO_2/Si, we find the peak positions of the W $4f_{7/2}$ orbital in elemental W at 31.7 eV and 32.3 eV for tungsten bonded to carbon. For WC transferred to SiO_2/Si, the W $4f_{7/2}$ positions are similar, with 31.5 eV for elemental tungsten and 32.2 eV for tungsten bonded to carbon. The contributions of metallic tungsten may arise from pieces of the Cu/W or Ga/W substrate that were not fully removed during the transfer process. We note that there is no evidence of tungsten oxides in any of these spectra as compared with reference data for tungsten oxides,[45,47,49] consistent with EDS mapping through STEM (Figure 3). We next turn to the C 1s regions of as-grown and transferred WC and W_2C, shown in Figure S8. In Figure S8a, we have the C 1s spectrum of as-grown W_2C/Ga/W, with peaks fit to many carbon species. Importantly here, we note that there is a small shoulder next to the sp^2 carbon peak that corresponds to carbon bonded to tungsten with reference values measured in the range 282.65-283.45 eV.[45,46] In WC/Cu/W, shown in Figure S8b, there are two primary contributions from graphitic carbon and C-O signal, as well as a small contribution from C-W near 283 eV. We note the significant differences in carbon species at the surface of both the gallium and copper substrates. Graphitic carbon is present in both samples, but the Ga/W substrate hosts an additional sp^3 carbon peak as well as a C=O contribution, reflecting the differences in methane decomposition over Ga versus Cu. Examining the transferred samples in Figure S8c and S8d, these spectra match well with the as-grown counterparts. While we observe the presence of tungsten-carbon bonding from XPS, consistent with structural characterization, we are unable to quantify the exact ratios of C/W here. First, the coverage of samples in these synthesis approaches is relatively small. Second, there is a large scattering cross section difference between X-rays and tungsten compared with carbon. This is complicated by the fact that there are ubiquitous carbon species across the substrate, mostly in the form of graphitic carbon as we discuss in the next section.

Assessment of process parameters on W_2C morphology and distribution

In the W_2C/Ga/W system, we investigated the influence of the quantity of Ar, H_2, and CH_4 on W_2C morphology and on the byproducts in the W_2C nanoplate synthesis. In Figure S9a-d we show representative SEM images of four conditions of W_2C growth—with and without H_2, and with 1 sccm CH_4 or 5 sccm CH_4. In the presence of H_2 at 5 sccm CH_4, we observe that platelets adopt a flat hexagonal morphology and are partially coalesced. By reducing the CH_4 flow rate to 1 sccm, still in the presence of H_2, we find that hexagonal platelets adopt a pyramid-like morphology. In the absence of H_2 at both 1 sccm and 5 sccm CH_4, we observe that the W_2C platelets begin to coalesce and increase in thickness. Moreover, there are brighter features in the SEM images shown at the border of these platelets and their aggregates; at the 1 sccm CH_4 growth condition in the absence of H_2, we also observe the presence of square pyramidal crystallites. To elucidate the growth of such features, we carried out EDS in SEM and found that these brighter crystallites are gallium oxide. Previous reports[50] and the Ga-O phase diagram[51] indicate that such gallium oxide is monoclinic β-Ga_2O_3, further confirmed in the XRD spectrum of as-grown W_2C/Ga/W in Figure S10. Analysis of the thermochemistry of the gallium/carbon/oxygen system revealed[52] that while H_2 is an effective reducing agent for Ga_2O_3 to Ga_2O at temperatures below 1100 °C, both CH_4 and carbon can reduce Ga_2O_3 as well, with CH_4 acting as a stronger reducing agent than H_2. The reduction of Ga_2O_3 is important in this process because under even parts per million O_2 content, which is inevitable in most atmospheric pressure CVD systems, Ga_2O_3 can form[42]. Moreover, at these high synthesis temperatures, stable Ga_2O_3 will crystallize. The growth of Ga_2O_3 on the gallium surface may inhibit lateral tungsten diffusion, as well as CH_4 reduction and subsequent carbon diffusion across the liquid gallium. We observe

that in the absence of H_2, while the W_2C platelets do seem to coalesce, compared to the synthesis in the presence of H_2, these gallium oxide crystallites are attached to the edges of the platelets. These relatively large crystallites may inhibit full coalescence of the W_2C platelets to form a film by limiting the tungsten and carbon diffusion to existing nucleation sites/carbide platelets. We also find that the gallium oxide crystals appear to attach to the edges of platelets with 1 sccm CH_4 in the presence of H_2, seen in the SEM images of two regions (Figure S11a,f) and corresponding oxygen maps (Figure S11b,g).

Another key aspect of the LMCVD synthesis of WC and W_2C that we investigate here is the simultaneous growth of the carbide and carbon species. Previous studies have demonstrated the growth of graphitic carbon with the LMCVD method, notably on Mo_2C on copper, and WC on both copper and gallium.[17,21,33] Figure 4 shows Raman spectra of as-grown WC/Cu/W, W_2C/Ga/W, as well as these samples transferred onto SiO_2/Si substrates. The Raman signal both on and off the WC flakes from Cu/W in 4a1) and 4b1) show the presence of D, G, and 2D bands corresponding to graphitic carbon. The peak position of the 2D band on and off WC, both as-grown and transferred, matches that of monolayer graphene.[53,54] Notably, there is a shift in the 2D band position on and off the WC flake. Further studies will be carried out to determine the origin of this shift. Also of note is the appearance of the D' peak post-transfer of the graphene/WC heterostructure. The wet transfer process has been shown to introduce defects in the graphitic carbon,[55] and we note this as the origin of these defects in the transferred graphene/WC. We next examine the Raman signal of the W_2C platelets from Ga/W shown in Figure 4c1) and 4d1). In the as-grown sample, we observe D and G bands corresponding to sp^2 amorphous carbon.[56,57] The Raman spectrum taken on the W_2C/Ga shows no apparent Raman signal. There could be strong coupling between the metallic W_2C and metallic Ga substrate which may quench the Raman signal. The lack of the 2D band both on and off the substrate could indicate poor crystallization of graphitic carbon owing to the low carbon solubility in gallium and relatively high hydrogen to methane ratio during the synthesis. The synthesis conditions for high-quality graphene *via* CVD synthesis and the LMCVD process necessitate larger carbon/hydrocarbon to hydrogen ratios promote higher quality graphitic carbon; higher quantities of hydrogen or reducing agents result in the degradation or elimination of graphite.[58,59] On the transferred W_2C sample, we find that there is an increased signal of the D and G bands both on and off the W_2C flake. In both regions on this transferred sample, we likely have contributions from both as-grown carbon as well as residues from the transfer process. In either case, we note that these observations *via* Raman identify the ribbon-like features and particle-like features, seen in the AFM images in Figure S1c, as graphitic carbon.

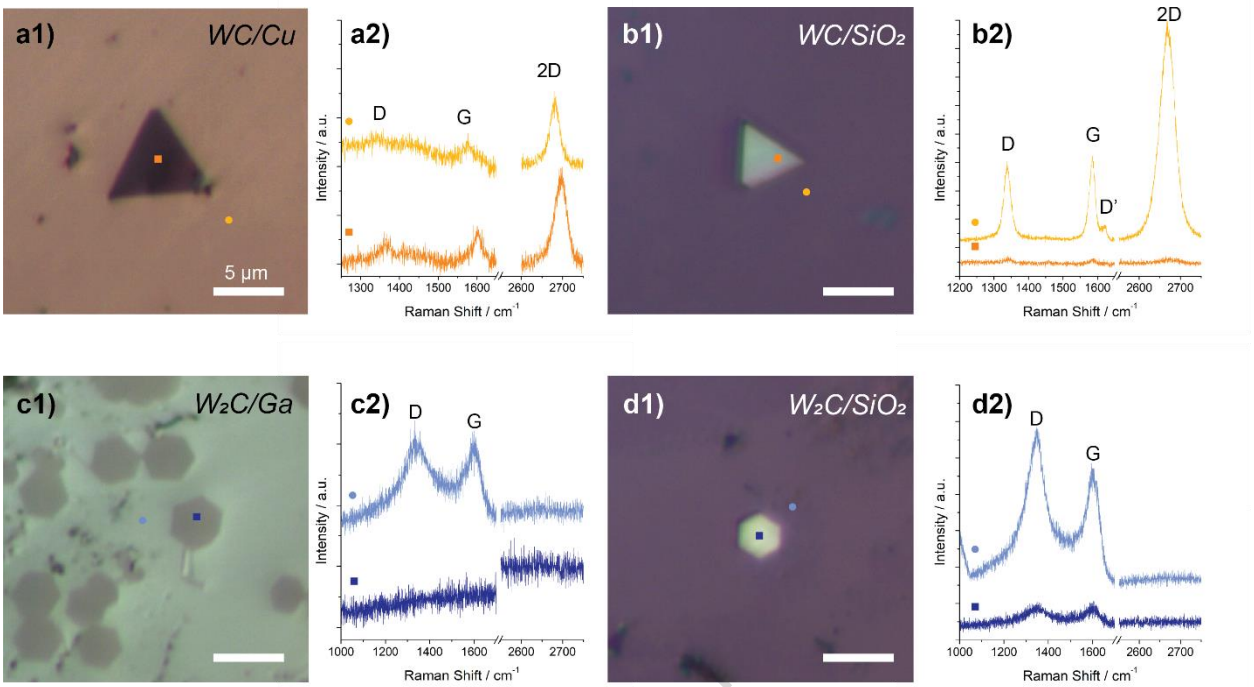

Figure 4: Raman spectroscopy of as-grown and transferred WC and W_2C nanoplates, from Cu/W and Ga/W respectively, onto SiO_2/Si. In all optical microscope images a-d1), scalebars are identical, and the lighter-shaded circle and darker-shaded square correspond to the respective location of the Raman spectra pictured in a-d2). In all optical microscope images, the lighter-shaded circle corresponds to spectra taken off the tungsten carbide flakes, and the darker-shaded square corresponds to Raman spectra taken on the tungsten carbide flake. The optical microscope images show a1) WC on Cu and b1) transferred to SiO_2/Si; c1) W_2C on Ga and d1) transferred to SiO_2/Si. Labels in the Raman spectra correspond to the D, G, D', and/or 2D bands of graphitic carbon.

Assessing the formation of distinct tungsten carbide phases

To assess the formation of the two tungsten carbide phases in the nanoplate morphology on different substrates, we investigated the thermodynamic properties of this system. According to the phase diagram,[60] bulk WC($P\bar{6}m2$) is thermodynamically favored under the reaction conditions in our system, and W_2C is metastable.[61] Our experimental analysis and data confirm that we do have these two phases, and this is confirmed by Density Functional Theory (DFT) calculations of various tungsten carbide phases (Figure S12a-e). In Figure S12f, we show the results of the calculation of the formation energy per atom (H_f) of tungsten carbide phases using bulk unit cells from the formula,

$$H_f = \frac{E - nE_W^{BCC} - mE_C^{sp^2}}{n+m} \quad (1)$$

where E is the total energy of the W_nC_m phase, n and m are the number of tungsten and carbon atoms (respectively) in the supercell, and E_W^{BCC} and $E_C^{sp^2}$ are the reference states for tungsten (body centered cubic) and carbon (sp^2, graphite), respectively. These results accurately reproduce the phase stability according to the phase diagram, as expected.

ARTICLE IN PRESS

One key difference between the two experimental setups is the diffusion barrier in the LMCVD process. We first observed that the density of gallium is less than that of copper (both in the liquid state).[62,63] With this in mind, we calculated the mean square displacement of tungsten atoms in a melt of gallium and copper (Figure S13a,b) near experimental temperatures (1173 K and 1367 K) using *ab initio* molecular dynamics simulations to investigate to investigate differences in the diffusion coefficients. The pair correlation function (Figure S13c) is used to extract the mean square displacement of tungsten in gallium (Figure S13d) and copper (Figure S13e), from which diffusion coefficients can be extracted. Our results indicate that while the diffusion coefficient of tungsten in gallium is greater than that of copper, they are still the same order of magnitude. These results are consistent with our observations of differences in the nucleation density of WC and W_2C platelets. A limitation in this calculation is that clustering of tungsten atoms during the diffusion process and the presence of Ga_2O_3 or other suboxide gallium species on the gallium substrate are not examined. We next considered a key difference between copper and gallium, their carbon solubility. Examining the carbon-copper binary phase diagram, carbon solubility in liquid copper is about 14 ppm (0.0076 wt%).[64] In gallium, there are no reported carbon-gallium phase diagrams owing to its nearly-negligible carbon solubility. However, gallium has been used in the synthesis of graphitic carbon and has been shown to graphitize carbon at its surface.[65–67] We also observed this in carburization of Ga/W in our system (Figure 4c,d). This reduced carbon solubility of gallium when compared to that of copper may explain the formation of the carbon-deficient (tungsten-rich) W_2C phase on Ga/W substrates. Considering this, we investigated the phase stability ordering with changes to the carbon chemical potential.

As revealed by TEM and SAED analysis, the basal plane of the WC corresponds to the (001) while that of W_2C corresponds to (200). Considering a slab model for each tungsten carbide phase (structures shown in Figure S14a-e), we find that the phase stability ordering changes for the carbon chemical potential. The presence of the (001) and (200) surfaces of hexagonal WC and orthorhombic W_2C are predicted to affect the stability of these nanostructures. We plot the deviation in formation energy, termed $\Delta\Phi$, defined in Equation (2) as

$$\Delta\Phi = H_f - \frac{n}{n+m}\Delta\mu_C \tag{2}$$

where $\Delta\mu_C$ is the deviation of carbon chemical potential μ_C from the reference state energy for graphite, $E_C^{sp^2}$. The relationship between $\Delta\Phi$ and $\Delta\mu_C$ is shown in Figure S15. We find that at highly carbon deficient conditions, W_2C in the $P\bar{3}1m$ and Pbcn polymorphs are more stable than WC ($P\bar{6}m2$). We can qualitatively relate these thermodynamic calculations to experimental observation. To explain this experimentally, we hypothesize that it is the difference in carbon solubility and methane pyrolysis activity between gallium and copper that leads to the formation of two distinct carbide phases in the nanoplate morphology. The precise flow rates of CH_4 in the synthesis of WC and W_2C are different but no more than 10 sccm in magnitude. In the thermodynamic calculation, we are interested in the local chemical potential of carbon at the substrate surface which from experiment is difficult to estimate. The total flow rate of CH_4 is not immediately linked to the chemical potential of carbon, because this chemical potential must be taken locally at the surface of the liquid metal substrate. Because copper has higher carbon solubility and can graphitize carbon more readily than gallium, we expect that these substrates host a carbon rich environment, relative to the gallium substrates. These findings are consistent with previous reports on the synthesis of transition metal borides and phase control *via* chemical potential modulation.[68] It is important to emphasize, however, that our analysis does not consider kinetic effects. While we claim that

ARTICLE IN PRESS

this thermodynamic consideration of tuning carbon chemical potential can explain the isolation of two tungsten carbides in the LMCVD process, a full picture should include kinetic considerations such as the carbon diffusion rate, both on the surface of and in the bulk of the liquid metal.

Electronic transport properties of WC and W_2C single crystals

Transition metal carbides are generally understood to be conventional type-II superconductors. Historically, these superconducting properties have been studied in bulk powder samples with ranges of reported transition temperatures and critical fields. This is attributed to variations in sample quality as well as phase.[29,30,69,70] For tungsten carbide, previous studies showed that the monocarbide WC ($P\bar{6}m2$) was not superconducting down to 300 mK and the semicarbides (W_2C) are superconducting below 4 K.[29,30,70] While anisotropic magnetoresistance has been observed in ultrathin single crystal WC ($P\bar{6}m2$) produced *via* LMCVD,[20] electronic transport properties were not probed below 300 mK, and no reports on the electronic transport properties of ultrathin W_2C exist to date. This provides motivation to systematically study electronic transport properties of both WC and W_2C.

We first examine the electronic transport of WC. An AFM image of the crystal and the device structure is shown in Figure 5a. This WC platelet has a measured thickness of about 20 nm (Figure S16c,d). We show the channel resistance (between probes labelled in Figure 5a) in response to an external out-of-plane magnetic field at 12 mK in Figure 5b. This resistance is a combination of transverse and longitudinal contributions due to the device geometry, with a minimum value of about 300 mΩ at zero magnetic field. The nonzero resistance in the absence of a magnetic field indicates that WC does not enter a superconducting state down to 12 mK. Additionally, the monotonic increase in resistance with increasing magnetic field is consistent with previous observations of ultrathin WC.[20] One explanation for the lack of

ARTICLE IN PRESS

observation of a superconducting state is the low density of states at the Fermi energy as calculated by DFT, shown in Figure S17.

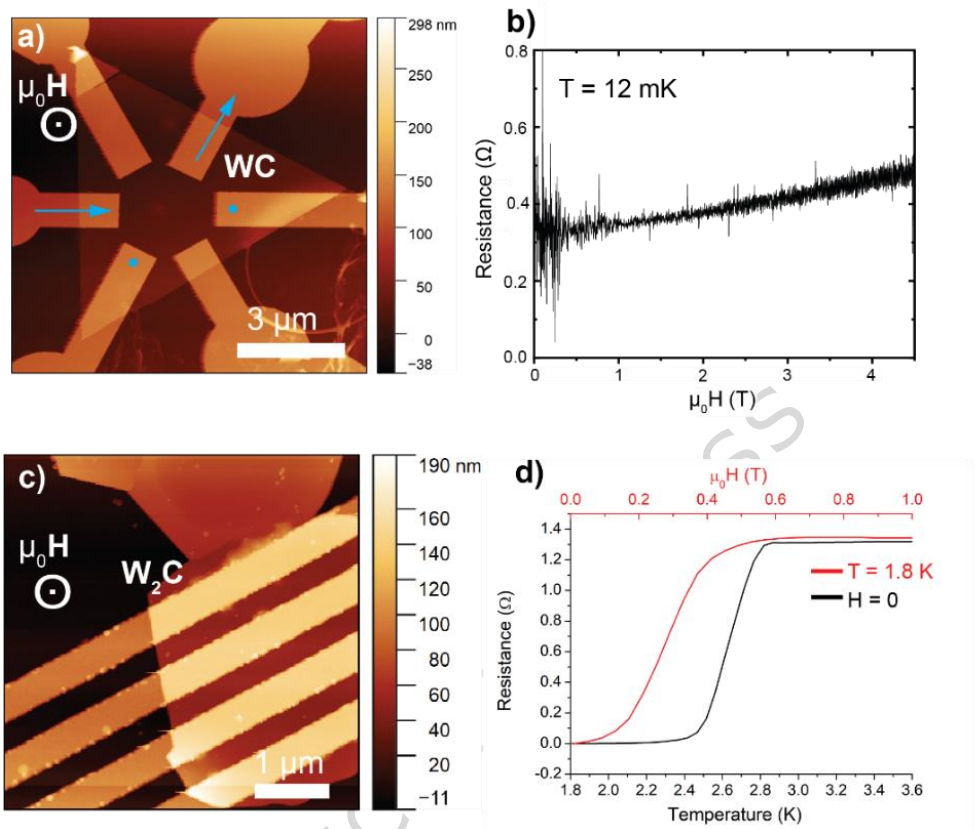

Figure 5: Longitudinal electronic transport in WC and W_2C. a) AFM image of WC device, where the arrows indicate source and drain, and the dots indicate the voltage terminals. b) Resistance measured across the voltage terminals as a function of applied magnetic field out-of-plane at a temperature of 12 mK. c) AFM image of W_2C device. d) Temperature dependence of resistance in the absence of magnetic field, and out-of-plane magnetic field dependence of resistance at a temperature of 1.8 K.

We have also probed the electronic transport properties of W_2C single crystals down to 1.8 K. Figure 5c shows an AFM image of the W_2C device. The platelet in this device has a thickness of around 51 nm (Figure S16a,b), and the resistance as a function of temperature and out of plane magnetic field is shown in Figure 5d. The W_2C crystal shows metallic behavior (dR/dT > 0) for the temperature range probed (Figure S18). We assign the superconducting transition temperature to the temperature at which the resistance of the material falls to 90% of its normal state resistance.[14] Using this criterion, we determine the transition temperature of the platelet in Figure 5c to be 2.8 K with a transition width of about 0.27 K, measured from the onset temperature and the temperature at which the resistance reaches 0 Ω. We also measure the resistive transition in a second W_2C platelet which shows similar superconducting behavior (Figure S19a-d). This superconducting transition temperature is consistent with those reported from previous studies of powder tungsten carbide samples.[30] It should be noted that early work on superconductivity in TMCs focused on carburized tungsten precursors, which can exhibit a range of composition, carbon concentration, and sample heterogeneity.[29,30,35,69] In this work, the W_2C nanoplates exhibit sharp superconducting transitions, similar to those reported for Mo_2C.[7] While thickness-dependent transport properties are not systematically studied here, we expect that W_2C will follow the same trends for other conventional type-II superconductors, such as Mo_2C.[7,14]

ARTICLE IN PRESS

We further probe the low temperature electronic transport properties of W_2C in Figure 6. We first apply an out-of-plane and in-plane magnetic field and measure the channel resistance, shown in Figure 6a and 6b, respectively. We find that the critical temperature shifts to lower values with increasing magnetic fields, as expected for type-II superconductors.[71] Moreover, the in-plane magnetic fields required to suppress the superconducting state are larger than the out-of-plane fields. We extract the temperature dependence of the upper critical magnetic field in the out-of-plane and in-plane directions, (Figure 6c and Figure S20a,b). According to linearized Ginzburg-Landau (GL) theory for 2D superconductors, the upper critical field out-of-plane will follow a linear dependence on temperature, as shown in Equation (3), where $\Phi_0 = h/2e$ is the flux quantum.[71] We fit the measured out-of-plane critical field to Equation (3) and extract the in-plane GL coherence length as $\xi_{\parallel}(0)$ =17 nm.

$$H_{c2,\perp}(T) = \frac{\Phi_0}{2\pi\xi_{\parallel}(0)^2}\left(1 - \frac{T}{T_c}\right) \tag{3}$$

$$H_{c2,\parallel}(T) = \frac{\sqrt{12}\Phi_0}{2\pi\xi_{\parallel}(0)\xi_{\perp}(0)}\sqrt{1 - \frac{T}{T_c}} \tag{4}$$

We next analyze the in-plane critical field temperature dependence. Figure 6c shows the in-plane critical field temperature dependence and its fit to the result from linearized GL theory shown in Equation (4)[71]. From this fit, we extract the out-of-plane GL coherence length as around 52 nm.

$$\left|\frac{H_{c2}(\theta)\cos\theta}{H_{c2,\perp}}\right| + \left(\frac{H_{c2}(\theta)\sin\theta}{H_{c2,\parallel}}\right)^2 = 1 \tag{5}$$

$$\left(\frac{H_{c2}(\theta)\cos\theta}{H_{c2,\perp}}\right)^2 + \left(\frac{H_{c2}(\theta)\sin\theta}{H_{c2,\parallel}}\right)^2 = 1 \tag{6}$$

We then probe the angular dependence of the critical field. We measure magnetoresistance curves at 1.8 K with magnetic fields applied at an angle with respect to the normal of the platelet, and we extract the angular dependence of the critical field as shown in Figure 6d. The measured data fits well with the Tinkham formula, derived for 2D superconducting systems, and shown in Equation (5).[71] From this fit, we find an anisotropy ratio of about 1.8. One key observation is the deviation of the measured data from the cusp. The tails of the data in Figure 6d match well with the Tinkham fit, though the data deviates from Equation (5) near $\theta = \pi/2$, lacking a cusp. To rule out the possibility of a mass anisotropy feature, we fit the 3D GL result for the angular dependence of critical fields from Equation (6), and the plot is shown in Figure 6d. We note that the 2D Tinkham fit is in better agreement with our data than the 3D fit with residual R^2 errors of 0.995 and 0.975, respectively. Further investigation is required to resolve this deviation of the critical field about the in-plane case, in particular an analysis of the GL penetration depth relative to the film thickness and Ginzburg-Landau coherence length could explain this difference.[72] Using the weak coupling limit of the Bardeen-Cooper-Schrieffer (BCS) theory,[73] we can estimate the GL penetration depth (in nanometers), as $\lambda_{GL}(0)$ [nm] = 64.2 $\sqrt{\rho/T_c}$, where ρ is the normal state resistivity in μΩ cm. To estimate the normal state resistivity, we use $R = \rho\ell/wd$ where ℓ is the channel length

(between the middle two electrodes), d is the platelet thickness (measured by AFM), and w is the channel width (across the edges of the platelet). Using the device in Figure 5c, we find that $\rho \approx 30.9$ μΩ cm, and consequently $\lambda_{GL}(0) \approx 210$ nm. We note that the platelet thickness is 51 nm, while the in-plane coherence length is 17 nm. Rather than satisfying the conventional criterion for 2D superconductivity that the film thickness is less than the penetration depth λ but smaller than the coherence length ξ,[72] $d < \lambda, \xi$, we find that $\xi < d < \lambda$. This behavior has been observed in superconducting niobium nitride films that also exhibited deviation from predicted angular dependence of the upper critical fields.[72] The in-plane magnetic field fully penetrates the nanoplatelet, resulting in 2D-like supercurrents in the platelet[74] but still retains some 3D character from the relative size of the coherence length to the platelet thickness. This is evidenced by the relatively small anisotropy ratio of the in-plane to out-of-plane critical fields. Equations 5 and 6 are ideal edge cases of 2D and 3D superconductivity, respectively, though our measurements indicate that we are in an intermediate regime. Further work is needed to study the exact nature of this crossover from 2D to 3D superconductivity, and to do this careful control over platelet thickness and lateral size is needed, a subject of further study.

Figure 6: Superconducting features of W_2C. Temperature dependence of resistance in response to a varying a) out-of-plane and b) in-plane magnetic field. Insets define the relevant directions of the magnetic field and [200] zone axis of the W_2C platelet. c) Temperature dependence of upper critical magnetic fields out-of-plane and in-plane. d) Angular dependence of upper critical magnetic field measured at a temperature of 1.8 K.

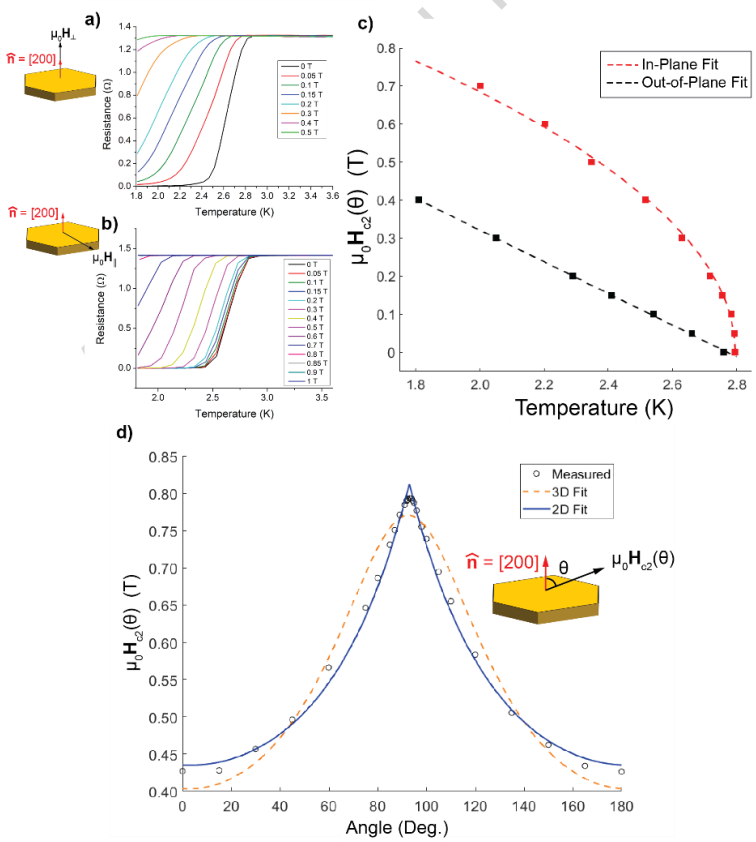

Discussion

In this study, we have controlled the synthesis of single crystal, tungsten carbide nanoplates in two phases through substrate modification: triangular WC ($P\bar{6}m2$) nanoplates on Cu/W substrates, and hexagonal W_2C (Pbcn) nanoplates on Ga/W substrates. A small contribution of W_2C aggregates is present in the

ARTICLE IN PRESS

synthesis of tungsten carbide on copper/tungsten substrates. The thickness of the nanoplates has been measured within the range of 20-100 nm. Moreover, we find that the ratio of methane and hydrogen is a critical parameter towards controlling platelet morphology. Key features of the W_2C synthesis include gallium oxide crystallites which may play a role in the growth of W_2C platelets. Thermodynamic considerations indicate that surface effects during nucleation as well as differences in carbon chemical potential on the liquid metal surfaces could lead to the formation of distinct tungsten carbide phases in the nanoplate morphology that can be modified through substrate choice. We also measured the low temperature electronic transport properties of ultrathin WC and W_2C nanoplates, and we found that while WC does not enter a superconducting state down to 12 mK, ultrathin W_2C crystals enter this state near 2.8 K. Semimetal WC is not superconducting likely because of its low density of states at the Fermi energy and weak electron-phonon coupling.[20] In W_2C, we find that the platelets behave like 2D superconductors with weak anisotropy, following a linear and square root dependence of out-of-plane and in-plane critical fields with temperature, respectively, similar to what has been observed in Mo_2C platelets.[7,14] The findings in this study lay groundwork towards modification of TMC phases through changes to the LMCVD diffusion barrier. Future work should investigate the use of other substrates in LMCVD synthesis of TMCs and transition metal nitrides (TMNs), while taking care to control the formation of other compounds in the synthesis. Additionally, thickness control in novel TMCs and TMNs would offer opportunities to investigate thickness dependent anisotropies and probe the boundaries of 2D and 3D-like superconducting behavior in TMCs and TMNs. The LMCVD technique could also be used for creating doped and alloyed TMCs and TMNs to further tailor emergent properties.

Methods

LMCVD synthesis of WC and W_2C. We adapt the methods of recent studies of LMCVD-grown tungsten carbide.[20,21] For WC synthesis, Cu foils are stacked on top of W foil; for W_2C synthesis, a 10 mg Ga shot is placed on the W foil. then loaded into an alumina crucible at the of a quartz tube furnace (Lindberg/Blue M). For the synthesis of WC, 10 mm x 10 mm x 25 um copper foil (Alfa Aesar, 99.8% metals basis, 25 µm thick) is placed on 10 mm x 10mm x 50 micron tungsten foil (Alfa Aesar, 99.95% metals basis, 50 µm thick). W and Cu foils are cleaned first in acetone, then isopropanol, then submerged in acetic acid (20 vol.%) for 10 minutes at 80°C. The substrates are then rinsed in deionized water. The W and Cu foils are stacked and pressed together manually using a glass slide. For the synthesis of W_2C, 10 mg liquid Ga (Beantown Chemical, Hudson NH, 99.9999% trace metals basis) is placed on a 5mm x 5mm x 50 um tungsten foil cleaned in acetone, isopropanol, then a 1:1 (by volume) solution of hydrochloric acid for 10 minutes, then rinsed in DI water. The substrate is placed into an alumina boat which is then placed into a quartz tube and loaded into the furnace. The furnace used for all experiments is a Mini-mite tube furnace (Lindberg Blue M); the quartz tubes used have length 1.3 m, inner diameter 27 mm, and outer diameter 28 mm. For the synthesis of WC, the furnace is set to 1090°C for 240 minutes under 500 sccm Ar/H_2 (85:15) and 10 sccm CH_4. For the synthesis of W_2C, the furnace is set to 1000°C for 30 minutes under 500 sccm Ar/H_2 (85:15) and 1-5 sccm CH_4. For the synthesis of both WC and W_2C, the furnace is initially purged under 500 sccm Ar/H_2 (85:15) for 20 minutes prior to the growth, and the furnace is rapidly cooled following the growth to avoid unwanted tungsten precipitation.

Transfer procedure

A polymethyl methacrylate (PMMA) assisted wet transfer was used to transfer the WC and W_2C platelets to either SiO_2/Si substrates or TEM grids (Au, Quantifoil) for further characterization. For both WC/Cu/W

ARTICLE IN PRESS

and W_2C/Ga/W, ~1 mL PMMA (495 A6) was dropped onto the substrate and subsequently spin coated at 4000 rpm for 45 seconds. The PMMA-coated samples were immediately placed onto a hot plate at 180°C for 90 seconds to cure the PMMA. Then, the edges of the substrates were cut to the desired size, and each was placed into an etchant bath. For WC/Cu/W, copper etchant (Thermo Scientific) at ambient temperature was used, and for W_2C/Ga/W, a 10% (by volume) solution of hydrochloric acid (Sigma-Aldrich, ACS reagent 37%) at 80°C was used. After the copper and gallium etched and the tungsten foil released, the floating PMMA/tungsten carbide was picked up with a glass slide and transferred into a deionized water bath. The PMMA/tungsten carbide was transferred to three additional water baths for 10-15 minutes each. A SiO_2/Si substrate or TEM grid was then used to pick up the PMMA/tungsten carbide at the last step, and then placed on a hot plate at 70°C for 10 minutes. To wash off the PMMA, samples were submerged in an acetone bath at 80°C for 60 minutes, then rinsed in isopropanol at room temperature for 10 minutes.

Characterization

Optical microscopy images were taken with a Zeiss optical microscope. SEM images were acquired on a XL30 ESEM (TSS Microscopy) using secondary electrons at 10 kV accelerating voltage. Cross-sectional TEM samples were prepared using a Scios 2 dual beam focused ion beam (Thermo Scientific). Prior to milling the samples with the gallium ion beam, a layer of amorphous carbon was deposited in the SEM to protect the surface of the nanoplate. Next an amorphous carbon layer was deposited, and trenches were milled using the gallium ion beam. The cross-section was lifted from the substrate, placed on a copper TEM grid (gold, Quantifoil), and thinned to electron transparency. HRTEM was performed on an FEI Talos F200X (Thermo Scientific) operated at 200 kV. EDS was acquired in STEM mode using a Super-X detector. EDS was analyzed and mapped using the Bruker ESPIRIT 2 software. TEM (SPECS). XPS measurements were performed using a Physical Electronics VersaProbe III system equipped with a monochromatic Al Kα X-ray source (hν = 1,486.7 eV) and a concentric hemispherical analyzer. High-resolution spectra were acquired from an analysis area with lateral dimension of ~200 µm. The C 1s and W 4f regions were collected at a pass energy of 27 eV, while the O 1s, Si 2p, Ga 3d, and Cu 2p regions were acquired at a pass energy of 55 eV. All spectra were fitted using Lorentzian line shapes with a Shirley background. Binding energies were charge-referenced to the sp^2-hybridized carbon peak in the C 1s region at 284.5 eV. XRD spectra acquired were from an Empyrean X-ray diffractometer in the Bragg-Brentano geometry (Malvern Panalytical) using copper $K\alpha_1$ X-rays (λ = 1.54061 Å). Raman spectra were collected using a confocal Raman microscope (HORIBA LabRAM HR Evolution) with linearly polarized, 532 nm laser excitation with 1800 gr mm^{-1} grating. Standard electron beam lithography techniques were used to pattern the tungsten carbide device structures. The contacts are composed of a 10 nm chromium bonding layer, followed by 100 nm gold. The W_2C electronic transport properties were measured in a physical property measurement system by Quantum Design with an excitation current of 10 µA with each data point averaged from 25 measurements, and the WC electronic transport properties were measured in a Bluefors LD250 cryogen-free dilution fridge with an AMI 9-1-1 T magnet with an excitation current (through the WC device) of 100 nA. The excitation current was sent in from a SR860 lock-in amplifier, and the output is filtered through with RC low frequency low-pass filters (QFilter) from Quantum Machines. The QFilter consists of 3 cascaded sections, each individually shielded, one reflective 7-pole pi filter and two dissipative RC filter stages.

Density functional theory calculation details

ARTICLE IN PRESS

All of the DFT calculations in this work were performed using the Vienna *ab initio* simulation package (VASP) code.[75] The effective core potentials were described by the projector augmented wave (PAW) potentials[76] with a cutoff energy of 600 eV. The Perdew–Burke–Ernzerhof (PBE) functionals[77] were used to describe the exchange-correlation interactions. The Monkhorst-Pack k-mesh was sampled with a density of 0.05 $Å^{-1}$. As for structure relaxation, BFGS quasi-Newton algorithm was used, and the thresholds of convergence were using 10^{-5} eV as break conditions for the electronic self-consistence loop and Hellmann-Feynman force on each atom is less than 0.01 eV $Å^{-1}$. The valence electron configurations are $6s^2 5d^4$ for W and $2s^2 2p^2$ for C. For all slab models, a 15 Å thickness of vacuum layer was used to eliminate interaction between neighboring supercells due to the periodic boundary conditions (PBCs). In addition, 9-atomic-layered WC was used as slab. We note that a 9-layer slab is considered sufficiently thick to eliminate interactions between the upper and lower surfaces.[78] Given the polar nature of the [0001] tungsten carbide surface, both W-termination and C-termination have been considered.

The diffusivity of tungsten in liquid copper and gallium was calculated using *ab initio* molecular dynamics (AIMD) as implemented in VASP. The simulation cells for liquid copper and liquid gallium consisted of 64 and 108 atoms, respectively, with one tungsten atom substituted into each system. Preliminary equilibration was performed in the NPT ensemble to adjust the internal pressure to approximately zero. Production simulations were then carried out in the NVT ensemble, with temperature controlled by a Nosé–Hoover thermostat.[79] The Mean squared displacement (MSD) of tungsten atoms was extracted from the AIMD trajectories, and the diffusivity D was computed using the Einstein relation:[80]

$$D = \lim_{t\to\infty} \frac{1}{6t} \langle |\boldsymbol{r}(t + t_0) - \boldsymbol{r}(t_0)|^2 \rangle. \quad (7)$$

where $r(t_0)$ denotes the MSD of tungsten atom at time t_0. As the time tends to infinity, the slope of the MSD versus time graph gives six times the diffusion coefficient.

ARTICLE IN PRESS

References

1. Kosolapova, T. Y. *Carbides*. (Plenum Press, New York, 1971).

2. Oyama, S. T. Preparation and Catalytic Properties of Transition Metal Carbides and Nitrides. *Catal. Today* **15**, 179–200 (1992).

ARTICLE IN PRESS

3. *The Chemistry of Transition Metal Carbides and Nitrides*. (Springer Netherlands, Dordrecht, 1996). doi:10.1007/978-94-009-1565-7.

4. Naguib, M. *et al.* Two-dimensional nanocrystals produced by exfoliation of Ti_3AlC_2. *Adv. Mater.* **23**, 4248–4253 (2011).

5. Shan, G., Ding, Z. & Gogotsi, Y. Two-dimensional MXenes and their applications. *Front. Phys.* **18**, 13604 (2023).

6. Gogotsi, Y. & Anasori, B. The Rise of MXenes. *ACS Nano* **13**, 8491–8494 (2019).

7. Xu, C. *et al.* Large-area high-quality 2D ultrathin Mo_2C superconducting crystals. *Nat. Mater.* **14**, 1135–1141 (2015).

8. Alhabeb, M. *et al.* Guidelines for Synthesis and Processing of Two-Dimensional Titanium Carbide (Ti3C2Tx MXene). *Chem. Mater.* **29**, 7633–7644 (2017).

9. Shekhirev, M., Shuck, C. E., Sarycheva, A. & Gogotsi, Y. Characterization of MXenes at every step, from their precursors to single flakes and assembled films. *Prog. Mater. Sci.* **120**, 100757 (2021).

10. Urbankowski, P. *et al.* Synthesis of two-dimensional titanium nitride $Ti_4 N_3$ (MXene). *Nanoscale* **8**, 11385–11391 (2016).

11. Wang, D. *et al. Direct Synthesis and Chemical Vapor Deposition of 2D Carbide and Nitride MXenes*. https://www.science.org.

12. Meshkian, R. *et al.* W-Based Atomic Laminates and Their 2D Derivative W1.33C MXene with Vacancy Ordering. *Adv. Mater.* **30**, 1706409 (2018).

13. Pan, H. Ultra-high electrochemical catalytic activity of MXenes. *Sci. Rep.* **6**, 32531 (2016).

14. Fan, Y. *et al.* Distinct superconducting properties and hydrostatic pressure effects in 2D α- and β-Mo_2C crystal sheets. *NPG Asia Mater.* **12**, 60 (2020).

15. Hart, J. L. *et al.* Control of MXenes' electronic properties through termination and intercalation. *Nat. Commun.* **10**, 522 (2019).

16. Bennett, L. H., Cuthill, J. R., McAlister, A. J., Erickson, N. E. & Watson, R. E. Electronic Structure and Catalytic Behavior of Tungsten Carbide. *Science* **184**, 563–565 (1974).

ARTICLE IN PRESS

17. Geng, D. C. *et al.* Direct synthesis of large-area 2D Mo2C on in situ grown graphene. *Adv. Mater.* **29**, 1700072 (2017).
18. Turker, F. *et al.* CVD synthesis and characterization of thin Mo2C crystals. *J. Am. Ceram. Soc.* **103**, 5586–5593 (2020).
19. Caylan, O. R. & Cambaz Buke, G. Low-temperature synthesis and growth model of thin Mo2C crystals on indium. *Sci. Rep.* **11**, 8247 (2021).
20. Wang, C. *et al.* Transport Properties of Topological Semimetal Tungsten Carbide in the 2D Limit. *Adv. Electron. Mater.* **5**, 1–7 (2019).
21. Zeng, M. *et al.* 2D WC single crystal embedded in graphene for enhancing hydrogen evolution reaction. *Nano Energy* **33**, 356–362 (2017).
22. Hao, M. *et al.* Transport through a network of two-dimensional NbC superconducting crystals connected via weak links. *Phys. Rev. B* **101**, 1–7 (2020).
23. Wang, Z. *et al.* Metal Immiscibility Route to Synthesis of Ultrathin Carbides, Borides, and Nitrides. *Adv. Mater.* **29**, 1–9 (2017).
24. Zhang, C. *et al.* Growth of self-aligned single-crystal vanadium carbide nanosheets with a controllable thickness on a unique staked metal substrate. *Appl. Surf. Sci.* **499**, 143998 (2020).
25. Sredenschek, A. J. *et al.* Heterostructures coupling ultrathin metal carbides and chalcogenides. *Nat. Mater.* **23**, 460–469 (2024).
26. Zhang, F. *et al.* Superconductivity enhancement in phase-engineered molybdenum carbide/disulfide vertical heterostructures. *Proc. Natl. Acad. Sci.* **117**, 19685–19693 (2020).
27. Ma, J. Z. *et al.* Three-component fermions with surface Fermi arcs in tungsten carbide. *Nat. Phys.* **14**, 349–354 (2018).
28. He, J. B. *et al.* Magnetotransport properties of the triply degenerate node topological semimetal tungsten carbide. *Phys. Rev. B* **95**, 195165 (2017).
29. Morton, N. *et al.* Superconductivity of Molybdenum and Tungsten Carbides. *J. -Common Met.* **25**, 97–106 (1971).

ARTICLE IN PRESS

ARTICLE IN PRESS

30. Morton, N., James, B. W., Wostenholm, G. H. & Hepburn, D. C. B. Superconductivity and the structure of W2C. *J. -Common Met.* **29**, 423–426 (1972).
31. Liu, Z. *et al.* Unique Domain Structure of Two-Dimensional α-Mo2C Superconducting Crystals. *Nano Lett.* **16**, 4243–4250 (2016).
32. Li, M. *et al.* Substrate Engineering toward Selective Growth of Ultrathin WC Crystals and Heterostructures via Liquid Cu-Zn Catalyst. *Adv. Funct. Mater.* **34**, 2316159 (2024).
33. Sun, W. *et al.* Controlled synthesis of 2D Mo2C/graphene heterostructure on liquid Au substrates as enhanced electrocatalytic electrodes. *Nanotechnology* **30**, 385601 (2019).
34. Liu, Z. *et al.* Phase transition and in situ construction of lateral heterostructure of 2D superconducting α/β Mo2C with sharp interface by electron beam irradiation. *Nanoscale* **9**, 7501–7507 (2017).
35. Kurlov, A. S. & Gusev, A. I. *Tungsten Carbides: Structure, Properties and Application in Hardmetals*. *Springer Series in Materials Science* vol. 184 (Springer International Publishing, Cham, 2013).
36. Toth, L. E. *Transition Metal Carbides and Nitrides*. (Academic Press, New York, 1971).
37. Msheik, M., Rodat, S. & Abanades, S. Methane cracking for hydrogen production: A review of catalytic and molten media pyrolysis. *Energies* **14**, 3107 (2021).
38. Sánchez-Bastardo, N., Schlögl, R. & Ruland, H. Methane Pyrolysis for Zero-Emission Hydrogen Production: A Potential Bridge Technology from Fossil Fuels to a Renewable and Sustainable Hydrogen Economy. *Ind. Eng. Chem. Res.* **60**, 11855–11881 (2021).
39. Kurlov, A. S. & Gusev, A. I. Tungsten carbides and W-C phase diagram. *Inorg. Mater.* **42**, 121–127 (2006).
40. Valvo, M., Thyr, J. & Edvinsson, T. Defect-Induced Raman Scattering in Cu_2 O Nanostructures and Their Photocatalytic Performance. *ChemElectroChem* **10**, e202300376 (2023).
41. Xiang, C. *et al.* Formation of stacking faults in tungsten carbide during sintering. *Ceram. Int.* **46**, 15851–15857 (2020).

ARTICLE IN PRESS

ARTICLE IN PRESS

42. Chabala, J. M. Oxide-growth kinetics and fractal-like patterning across liquid gallium surfaces. *Phys. Rev. B* **46**, 11346–11357 (1992).

43. Holmes, R., O'Neill, H. S. C. & Arculus, R. Standard Gibbs free energy of formation for Cu20, NiO, COO, and Fe,O: High resolution electrochemical measurements using zirconia solid electrolytes from 900-1400 K.

44. Zinkevich, M. & Aldinger, F. Thermodynamic Assessment of the Gallium-Oxygen System. *J. Am. Ceram. Soc.* **87**, 683–691 (2004).

45. Moulder, J., Stickle, W., Sobol, P. & Bombden, K. *Handbook of X-Ray Photoelectron Spectroscopy*. (Perkin-Elmer, 1992).

46. Krasovskii, P. V. *et al.* XPS study of surface chemistry of tungsten carbides nanopowders produced through DC thermal plasma/hydrogen annealing process. *Appl. Surf. Sci.* **339**, 46–54 (2015).

47. Katrib, A., Hemming, F., Wehrer, P., Hilaire, L. & Maire, G. The multi-structure of oxidized-reduced tungsten carbide surface(s). *Catal. Lett.* **29**, 397–408 (1994).

48. Leclercq, G. *et al.* Study of the Preparation of Bulk Powder Tungsten Carbides by Temperature Programmed Reaction with CH4+ H2Mixtures. *J. Catal.* **158**, 142–169 (1996).

49. Brillo, J., Kuhlenbeck, H. & Freund, H.-J. Interaction of O2 with WC(0001). *Surf. Sci.* **409**, 199–206 (1998).

50. Takezawa, K., Lu, J., Numako, C. & Takami, S. One-step solvothermal synthesis and growth mechanism of well-crystallized β-Ga2O3nanoparticles in isopropanol. *CrystEngComm* **23**, 6567–6573 (2021).

51. Okamoto, H. Ga-O (Gallium-Oxygen). *J. Phase Equilibria Diffus.* **29**, 550–551 (2008).

52. Saedi, M., Mohseni, S. M. & Groot, I. M. N. Thermodynamic analysis of graphene CVD grown on liquid metal: Growth on liquid metallic gallium or solid gallium oxide skin? *Mater. Chem. Phys.* **275**, 125203 (2022).

53. Ferrari, A. C. & Basko, D. M. Raman spectroscopy as a versatile tool for studying the properties of graphene. *Nat. Nanotechnol.* **8**, 235–246 (2013).

ARTICLE IN PRESS

ARTICLE IN PRESS

54. Ferrari, A. C. Raman spectroscopy of graphene and graphite: Disorder, electron-phonon coupling, doping and nonadiabatic effects. *Solid State Commun.* **143**, 47–57 (2007).
55. Ahmad, W., Ullah, Z., Sonil, N. I. & Khan, K. Introduction, production, characterization and applications of defects in graphene. *J. Mater. Sci. Mater. Electron.* **32**, 19991–20030 (2021).
56. Thapliyal, V. A concise review of the Raman spectra of carbon allotropes. *Diam. Relat. Mater.* **127**, 109180 (2022).
57. Yuan, R. *et al.* Raman spectroscopy analysis of disordered and amorphous carbon materials: A review of empirical correlations. *Carbon* **238**, 120214 (2025).
58. Wu, B. *et al.* Self-organized graphene crystal patterns. *NPG Asia Mater.* **5**, e36–e36 (2013).
59. Zhang, X. *et al.* Hydrogen-induced effects on the CVD growth of high-quality graphene structures. *Nanoscale* **5**, 8363 (2013).
60. Okamoto, H. C-W (Carbon-Tungsten). *J. Phase Equilibria Diffus.* **29**, 543–544 (2008).
61. Fernandes, C. M. & Senos, A. M. R. Cemented carbide phase diagrams: A review. *Int. J. Refract. Met. Hard Mater.* **29**, 405–418 (2011).
62. Assael, M. J. *et al.* Reference data for the density and viscosity of liquid copper and liquid tin. *J. Phys. Chem. Ref. Data* **39**, 033105 (2010).
63. Chentsov, V. P., Shevchenko, V. G., Mozgovoi, A. G. & Pokrasin, M. A. Density and surface tension of heavy liquid-metal coolants: Gallium and indium. *Inorg. Mater. Appl. Res.* **2**, 468–473 (2010).
64. C (Carbon) Binary Alloy Phase Diagrams. in *Alloy Phase Diagrams* (eds Okamoto, H., Schlesinger, M. E. & Mueller, E. M.) 218–228 (ASM International, 2016). doi:10.31399/asm.hb.v03.a0006151.
65. Fujita, J., Ueki, R., Miyazawa, Y. & Ichihashi, T. Graphitization at interface between amorphous carbon and liquid gallium for fabricating large area graphene sheets. *J. Vac. Sci. Technol. B Microelectron. Nanometer Struct. Process. Meas. Phenom.* **27**, 3063–3066 (2009).
66. Ueki, R. *et al.* In-situ observation of surface graphitization of gallium droplet and concentration of carbon in liquid gallium. *Jpn. J. Appl. Phys.* **51**, 06FD28 (2012).

ARTICLE IN PRESS

ARTICLE IN PRESS

67. Wang, J. *et al.* High-mobility graphene on liquid p-block elements by ultra-low-loss CVD growth. *Sci. Rep.* **3**, 2670 (2013).

68. Si, J. *et al.* Chemical Potential-Modulated Ultrahigh-Phase-Purity Growth of Ultrathin Transition-Metal Boride Single Crystals. *J. Am. Chem. Soc.* **145**, 3994–4002 (2022).

69. Willens, R. H. & Buehler, E. The superconductivity of the monocarbides of tungsten and molybdenum. *Appl. Phys. Lett.* **7**, 25–26 (1965).

70. Willens, R. H., Buehler, E. & Matthias, B. T. Superconductivity of the transition-metal carbides. *Phys. Rev.* **159**, 327–330 (1967).

71. Tinkham, M. *Introduction to Superconductivity*. (1996).

72. Belogolovskii, M. *et al.* Competing length scales and 2D versus 3D dimensionality in relatively thick superconducting NbN films. *Sci. Rep.* **13**, (2023).

73. Critical Fields, Pauli Paramagnetic Limiting, and Material Parameters of Nb3Sn and V3Si.

74. Schmidt, V. *The Physics of Superconductors:* (1997).

75. Kresse, G. & Furthmüller, J. Efficiency of ab-initio total energy calculations for metals and semiconductors using a plane-wave basis set. *Comput. Mater. Sci.* **6**, 15–50 (1996).

76. Kresse, G. & Joubert, D. *From Ultrasoft Pseudopotentials to the Projector Augmented-Wave Method*.

77. Perdew, J. P., Burke, K. & Ernzerhof, M. Generalized Gradient Approximation Made Simple. *Phys. Rev. Lett.* **77**, 3865–3868 (1996).

78. Li, Y. *et al.* Theoretical study on the electronic properties and stabilities of low-index surfaces of WC polymorphs. *Comput. Mater. Sci.* **50**, 939–948 (2011).

79. Nosé, S. A unified formulation of the constant temperature molecular dynamics methods. *J. Chem. Phys.* **81**, 511–519 (1984).

80. Einstein, A. & Statchel, J. (eds.). On the movement of small particles suspended in stationary liquids required by the molecular-kinetic theory of heat. in *The collected papers of Albert Einstein : English translation supplement* 123–134 (Princeton Univ. Press, Princeton, NJ, 1905).

ARTICLE IN PRESS

ARTICLE IN PRESS

Acknowledgements

This work was primarily supported by the Basic Office of Science of the Department of Energy under award number DE-SC0018025. Crystal structures generated using CrystalMaker, CrystalMaker Software Ltd, Oxford, England (www.crystalmaker.com). The schematic in Figure 1a was made in Adobe Dimension. The authors are grateful to the Materials Characterization Laboratory at the Pennsylvania State University.

Author contributions

M.T. and S.B.S. supervised the project. A.S. led the experimental design, sample preparation, and electronic transport analysis, and wrote the original manuscript draft. D.S. assisted with optimization of synthesis parameters, carried out planar and cross-sectional S/TEM, EDS, SAED, and led the crystal structure analysis. J.W. performed and led DFT calculations with experimental corroboration with A.S. and D.S.. D.Z. measured four-probe electronic transport in W_2C platelets with in-plane and angle-dependent magnetic fields; out-of-plane magnetic field measurements were done by A.S.. Z.Y. measured and analyzed AFM data for transferred WC and W_2C in addition to the devices used for electronic transport. Z.Y. also measured and analyzed the XPS spectra of as-grown and transferred WC and W_2C. L.Y. carried out electron beam lithography and evaporation of metal contacts to fabricate the WC and W_2C devices, and performed the low temperature electronic transport properties of WC under the supervision of M.K.. M.T., S.B.S., and M.K. revised and discussed the manuscript. All authors read, edited, and approved the final manuscript.

Competing interests

Mauricio Terrones is an Editorial Board Member of *npj 2D Materials and Applications*. Mauricio Terrones was not involved in the journal's review of, or decision related to, this manuscript. The other authors declare no competing financial or non-financial interests.

Supporting information available

Supporting information includes optical images, AFM, lateral size and thickness distributions, HRTEM with Fourier transforms and simulated SAED patterns, cross sectional HRTEM and corresponding Fourier transforms, Raman spectra, and XPS spectra of triangular WC and hexagonal W_2C nanoplates from Cu/W and Ga/W substrates, respectively. Also shown are representative SEM images of hexagonal W_2C nanoplates synthesized under various growth parameters, XRD of as-grown W_2C/Ga/W, SEM/EDS analysis of as-grown W_2C/Ga/W, crystal structures and corresponding CIF files with equation of state for tungsten carbide phases, calculations of mean square displacement used to determine diffusivity of tungsten in liquid copper and gallium, slab models and formation energies of tungsten carbide phases with varying carbon chemical potential, AFM images and linescans of WC and W_2C, density of states in tungsten carbide phases, temperature dependence of resistance of W_2C device across full temperature range, superconducting features of a second W_2C device, and two probe resistance of W_2C device with magnetoresistance.

Data availability statement

The authors declare that all data supporting the findings and conclusions of this work are found in the article and supplementary information. Additional data relating to this study is available upon reasonable request by the corresponding author.

ARTICLE IN PRESS

ARTICLE IN PRESS